RSC Advances

ROYAL SOCIETY OF CHEMISTRY

www.rsc.org/advances

Graphical abstract

The controlling synthesis and improved electrochemical cycleability of Mn-doped α-Fe_2O_3 hollow porous quadrangular prisms as lithium-ion battery anodes

Xinru Liu, Chenhao Zhao, Fan Feng, Faqi Yu, Wenpei Kang[1] and Qiang Shen*

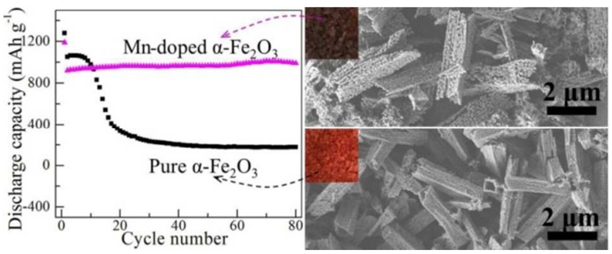

Shown is the controlling synthesis of anode material Mn-doped α-Fe_2O_3 hollow porous quadrangular prisms with an enhanced electrochemical cycling stability.

The controlling synthesis and improved electrochemical cycleability of Mn-doped α-Fe_2O_3 hollow porous quadrangular prisms as lithium-ion battery anodes

Xinru Liu, Chenhao Zhao, Fan Feng, Faqi Yu, Wenpei Kang[1] and Qiang Shen*

Key Laboratory for Colloid and Interface Chemistry of Education Ministry, School of Chemistry and Chemical Engineering, Shandong University, Jinan 250100, China.

*Corresponding authors: tel.: +86-531-88361387; fax: +86-531-88364464; e-mail: qshen@sdu.edu.cn.

[1] Present address: Department of Physics and Materials Science and Center of Super-Diamond and Advanced Films (COSDAF), City University of Hong Kong (P. R. China); also for correspondence (kwpsdu@163.com).

ABSTRACT

A two-step process of initial oxalate co-precipitation and subsequent thermal decomposition facilitates the formation of hydrated oxalate precursors with a shape of hollow quadrangular prism and then confers a porous nature for the prismatic shells of synthetic hematite (α-Fe_2O_3) and its Mn-doped derivative. When applied as lithium-ion battery anodes, Mn-doped α-Fe_2O_3 exhibits an improved electrochemical performance compared with undoped α-Fe_2O_3. At a current density of 200 mA g^{-1}, pure α-Fe_2O_3 electrode gives an initial discharge capacity of ~1280 mAh g^{-1} with a low retention ratio of 13.9% (i.e., capacity~178 mAh g^{-1}) over 80 cycles, while the Mn-doped product of rhombohedral $Fe_{1.7}Mn_{0.3}O_3$ delivers a relatively low initial value of ~1190 mAh g^{-1} and retains the 80th reversible capacity of ~1000 mAh g^{-1} (i.e., retention ratio~84.0%). These, together with the better high-rate capability and the lower charge-transfer resistance of Mn-doped α-Fe_2O_3 anode, simultaneously demonstrate a successful mass production of hollow porous configurations and an effective doping of elemental Mn for potential applicability purposes.

1. Introduction

Rechargeable lithium-ion batteries (LIBs) have been desired for low price, safety, high energy and high power to meet the requirements of large-scale applications, such as hybrid vehicles, electric vehicles and smart electric grids, and have prompted tremendous research efforts to investigate the controlling synthesis and improved performance of electrode materials with high-capacity or high-voltage.[1,2] As commercial anode material, natural or synthetic graphite possesses a low theoretical lithium storage capacity of 372 mAh g^{-1} and is far from the demands of high energy-storage devices. To substitute for this conventional carbonaceous material, transition metal oxides have ever been regarded as desired candidates owing to both the facile preparation of an ordered structure and their high theoretical lithium storage capacity.[3-10]

As one of iron oxides, hematite α-Fe_2O_3 is of natural abundance, low-cost, eco-friendliness and can be defined as a promising LIB anode material because of its high theoretical lithium storage capacity (1005 mAh g^{-1}).[3,5,11,12] In spite of the exoergic nature of conversion reactions, α-Fe_2O_3 has a pristine drawback of poor electronic and Li^+-ion conductivity for energy storage. As far as we know, both the shape- or size-controlled synthesis of nanostructured products[5,11-20] and the amorphous carbon- or graphene-coated treatment of transition metal oxides can solve the disadvantage by shorting Li^+-diffusion route or improving charge transfer kinetics.[21-27] Furthermore, partial substitution of another transition metal or elemental doping of alkaline earth metal can also improve the conductivity of transition metal oxide-based anodes, for instance, Co-doped Mn_3O_4 and NiO, Cu-doped Mn_2O_3, CoO and V_2O_5 and K^+-doped Co_3O_4 significantly exhibit a superior cycling stability compared with the corresponding undoped ones.[28-33] Up to now, there are few reports concerning about the metal-ion doping of potential anode material α-Fe_2O_3, let alone its shape-controlled and Mn-doped preparation simultaneously.

In this paper, initial oxalate co-precipitation at room temperature and subsequent thermal decomposition at 600°C were combinedly used for the controlling syntheses of undoped and Mn-doped α-Fe_2O_3 possessing a shape of hollow quadrangular prism with porous shell. An effective doping of elemental Mn in α-Fe_2O_3 crystal lattice and the similar structural parameters of undoped and Mn-doped samples facilitate their comparative electrochemical measurements as LIB anodes, which will be discussed in detail in context.

2. Experimental

2.1. Material synthesis

All the chemicals are of analytical grade and were used without any further purification. At first, oxalate precursors were precipitated from the reaction systems of ethylene glycol (EG, 5.0 mL), ultrapure water (18.2 MΩ·cm, 50.0 mL), excess sodium oxalate ($Na_2C_2O_4$, 3.0 mmol), iron sulfate hydrate ($FeSO_4 \cdot 7H_2O$, 1.8 or 1.5 mmol) and manganese sulfate hydrate ($MnSO_4 \cdot H_2O$, 0.0 or 0.3 mmol).[34] And then, the subsequent air-atmosphere heat-treatment of hydrated oxalate precursors were performed at 600 ^{o}C for 4 h, resulting in undoped α-Fe_2O_3 and its Mn-doped derivative $Fe_{1.7}Mn_{0.3}O_3$, respectively.

2.2. Structural characterization

The crystallographic information of oxalate precursors and their corresponding oxides was obtained using a Rigaku D/max-2400 powder X-ray diffractometer with Cu Ka radiation (40 kV, 120 mA). The chemical composition of Mn-doped α-Fe_2O_3 was determined using an inductively coupled plasma/atomic emission spectrometer (ICP/AES) on an IRIS Intrepid II XSP instrument. The morphology and structural feature of samples were examined using a JEOL JSM-6700F scanning electron microscopy (SEM). Thermogravimetry/differential scanning calorimetry (TGA/DSC) measurements were carried out on a Mettler apparatus under air atmosphere at a heating step of 10 °C min^{-1} from ambient temperature to 800 °C. Specific surface area and porosity of final oxides were measured on a Micromeritics ASAP 2020 sorptometer.

2.3. Electrochemical characterization

All the electrochemical experiments were performed at 30 ^oC using α-Fe_2O_3/Li coin cells (CR 2032) with lithium foil as counter electrode, celgard 2300 polymeric films as separators, and commercial LBC 305-01 $LiPF_6$ solution as electrolyte. The aqueous slurry was formed by the mixing of active materials, binder sodium alginate, acetylene black at a weight ratio of 70 : 10 : 20, cast onto copper foils, dried at 80 ^oC for 12 h, cut into discs and then used as a working electrode with a mass loading of 1.3 ± 0.1 mg cm^{-2}. The coin cells were assembled in an argon-filled glove box. Galvanostatic discharge-charge cycling tests were carried out on a Land CT2001A battery tester at various current densities within 0.01-3 V (*vs*. Li^+/Li and hereafter). Cyclic voltammetry (CV) measurements were performed on a LK 2005A Electrochemical Workstation between 0.01 and 3 V at a scanning rate of 0.1 mV s^{-1}. Electrochemical impedance spectroscopy (EIS) tests were carried out on a Zahner IM6 electrochemical workstation at frequencies ranging from 100 kHz to 0.1 Hz under the AC voltage amplitude of ± 5 mV.

3. Results and discussion

3.1. Preparation and structural characterization

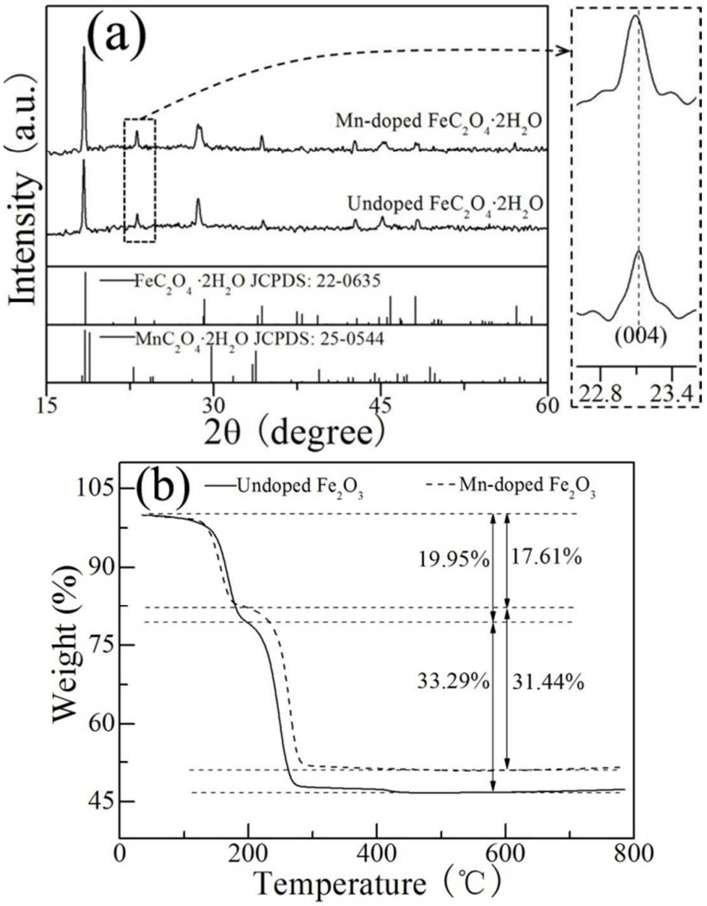

Fig. 1 (a) XRD patterns and (b) TGA profiles of undoped and Mn-doped oxalate precursors, and in panel (a) the diffraction peaks within the 2Thelta range of 22.6 and 23.6° was magnified and indexed according to the standard (004)-reflection data of orthorhombic $FeC_2O_4{\cdot}2H_2O$.

According to literature results, hollow microstructures of crystalline $FeC_2O_4{\cdot}2H_2O$ could be obtained from a mixed medium of ethylene glycol and water based on the water-assisted etching formation step.[34] After the precipitation of yellowish oxalate precursors, the resulting supernatants were greenish in color no matter the Mn(II)-containing raw material was previously added or not. That is, the so-called water-assisted etching formation step could also be adopted for the doping of elemental Mn, owing to the slight difference between the solubility product of $FeC_2O_4{\cdot}2H_2O$ (3.2×10^{-7}) and that of $MnC_2O_4{\cdot}2H_2O$ (1.7×10^{-7}). Furthermore, this was further developed for the skeleton-replicative transformation of Mn(II)-doped oxalate precursors to Mn(III)-doped iron(III) oxide porous nanostructures.

Fig. 1a shows the XRD patterns of undoped and Mn-doped oxalate precursors. Both the yellowish precipitates display almost the same XRD patterns and could be indexed by the standard reflection data of orthorhombic $FeC_2O_4{\cdot}2H_2O$ (JCPDS No. 22-0635) with no obvious diffraction peaks of monoclinic $MnC_2O_4{\cdot}2H_2O$ (JCPDS No. 25-0544). By magnification, there is a slight peak shift for the (004) crystal plane of orthorhombic $FeC_2O_4{\cdot}2H_2O$, indicating the effective doping of Mn(II) ions within the hydrated oxalate lattices (Fig. 1a).

TGA thermal properties of the two oxalate precursors are shown in Fig. 1b, which coincides well with literature results and gives the similar TGA curves with two major weight loss steps.[35,36] In Fig.1b the first weight loss below 185 ^{o}C corresponds to the loss of physically and chemically adsorbed water, while the second one around 251 ^{o}C is prominent and can be attributed to the thermal decomposition of oxalate precursors. As shown in Fig. 1b, the undoped oxalate precursor exhibits an initial weight loss of ~20.0% and a subsequent one of ~33.3%, while the Mn-doped $FeC_2O_4{\cdot}2H_2O$ presents the two weight losses at a value of ~17.6% and 31.4%, respectively. Considering the different atomic ratios of M^{2+} (M = Fe, Mn) ions and the different molecular weight of $MC_2O_4{\cdot}2H_2O$, these confirm the effective doping of Mn(II) ions within the hydrated oxalate lattices (Fig. 1b).

Under air atmosphere, the thermal decompositions of undoped and Mn-doped precursors can be simply described as the following chemical formula: [19,36]

$$4MC_2O_4\cdot 2H_2O \xrightarrow{500\sim700^{o}\,C} 2M_2O_3 + 2CO_2 + 6CO + 8H_2O \qquad (1)$$

According to the TGA results, a heat-treatment temperature of 600 °C was selected for the preparation of undoped and Mn-doped α-Fe_2O_3 samples (Fig. S1-3).[19,36] After the thermal decomposition of Mn-doped oxalate precursors at 600 °C, the Fe/Mn elemental ratio was determined by ICP/AES method, giving a chemical formula of $Fe_{1.7}Mn_{0.3}O_3$ for the resulting Mn-doped α-Fe_2O_3 sample. XRD patterns of both undoped and Mn-doped samples match well with the standard reflection data of rhombohedral α-Fe_2O_3 (JCPDS No. 33-0664) as shown in Fig. 2. Therein, the magnified (116)-face reflections of rhombohedral crystal phase indicate that there is almost no peak shifting for the doped sample of $Fe_{1.7}Mn_{0.3}O_3$. In some sense, this suggests that elemental Mn is highly dispersed in the matrix of crystalline α-Fe_2O_3.

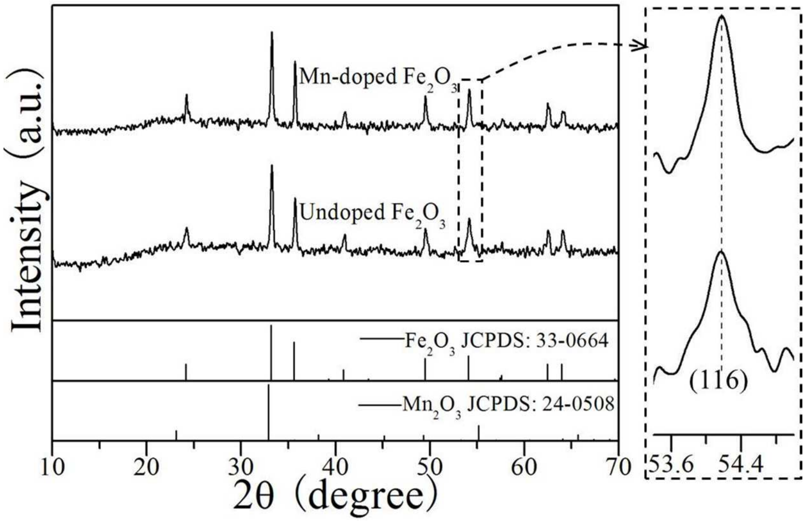

Fig. 2 XRD patterns of undoped and Mn-doped α-Fe_2O_3 samples, and the diffraction peaks within the 2Thelta range of 53.4 and 55.0° was magnified and indexed according to the standard (116)-reflection data of rhombohedral α-Fe_2O_3.

SEM observation shows that both the undoped and Mn-doped oxalate precursors acquire sharp edges, irregular sizes and a shape of hollow quadrangular prism (Fig. 3a, b). It is due to the time-dependent etching of water that few configurations could possess a thin skeleton and would be mechanically broken thereafter.[34] Through the 4-h decomposition of these oxalate precursors at 600°C, the final oxides (i.e., pure Fe_2O_3 and $Fe_{1.7}Mn_{0.3}O_3$) conserves the structural skeletons and sizes of corresponding oxalate precursors, as shown in Fig. 3c and d. Also, a porous feature of shells, as well as the crystallinity and structural integration of resulting oxides M_2O_3 (M = Fe or $Fe_{1.7}Mn_{0.3}$), can be successfully achieved at the selected calcination temperature (Fig. S1, S2 and S3). In Fig. 3c and d, the inserted digital photographs comparatively show that the color of $Fe_{1.7}Mn_{0.3}O_3$ powders is deeper than that of pure Fe_2O_3, confirming the formation of Mn-doped α-Fe_2O_3 combined with their comparative analysis of XRD patterns shown in Fig. 2.

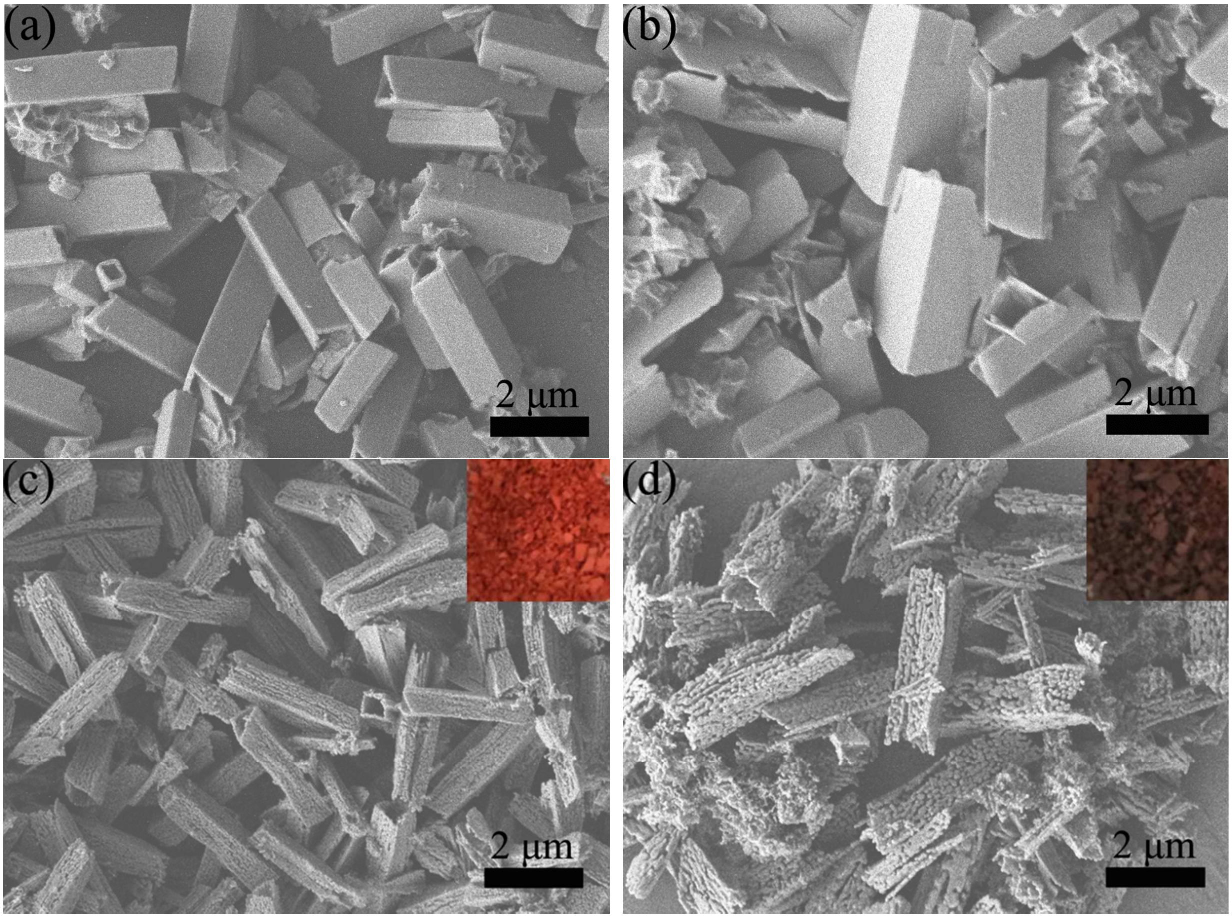

Fig. 3 SEM images of oxalate precursors and their decomposed products: (a), undoped $FeC_2O_4 \cdot 2H_2O$; (b), Mn-doped $FeC_2O_4 \cdot 2H_2O$; (c), undoped α-Fe_2O_3; (d), Mn-doped α-Fe_2O_3. In panel (c) and (d), insets are the corresponding digital photographs of final products.

The comparison of Fig. 3b with 3d shows that, after the solid-state chemical transformation of oxalates to oxides, the shells of $Fe_{1.7}Mn_{0.3}O_3$ hollow quadrangular prisms are aggregates composed of nanoparticles. Simultaneously, according to above listed equation (1) the release of gases may randomly endow with interspaces among the nanoparticles of each prismatic shell. N_2 adsorption-desorption isotherms (i.e., Brunauer-Emmett-Teller, abbreviated as BET, isotherms) are comparatively shown in Fig. 4, exhibiting the specific surface areas of 11.55 and 11.48 $m^2 g^{-1}$ for pure α-Fe_2O_3 and its Mn-doped derivative, respectively. Insets in Fig. 4 are the corresponding pore size distribution estimated using Barrett-Joyner-Halenda (BJH) method, giving polydisperse pore diameters with an average value of 3.4 and 3.7 nm for undoped and Mn-doped α-Fe_2O_3 samples, respectively.

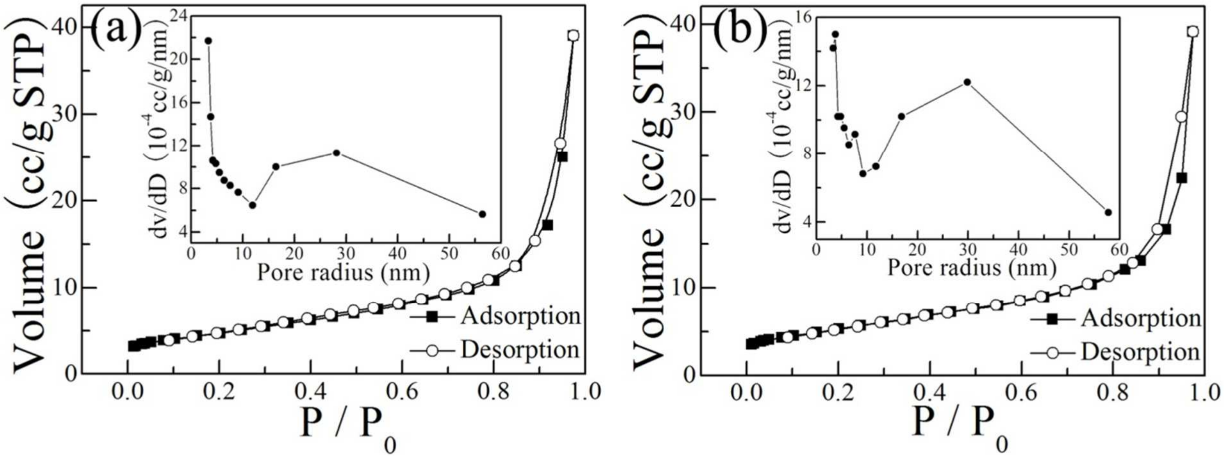

Fig. 4 N_2 adsorption-desorption isotherms of (a) undoped and (d) Mn-doped α-Fe_2O_3 samples and insets are the corresponding pore size distributions.

3.2. Enhanced electrochemical properties for LIB anodes

When applied as LIB anodes within the voltage range of 0.01-3 V, at 200 mA g^{-1} the discharge-charge profiles of pure α-Fe_2O_3 and Mn-doped α-Fe_2O_3 (i.e., $Fe_{1.7}Mn_{0.3}O_3$) are shown in Fig. 5a and b, respectively. Their initial discharge curves are similar and can be divided into four regions, marked as I, II, III and IV. On the principle of α-Fe_2O_3 conversion reaction mechanism reported previously,[16,21] if regions I-III correspond to the stepwise reduction of M^{3+} to M^0 (M = Fe or Fe-Mn) and denote the theoretical lithium storage capacity during the first discharging process, and then the sloped region IV relates to the size and surface area of as-obtained sample and may represent the extra lithium storage capacity observed therein. Also, both the discharge and charge plateau voltages in the 2nd voltage profile are higher than those in the initial one (Fig. 5a, b). Furthermore, almost all the 50th voltage plateaus (i.e., I-IV regions) of pure α-Fe_2O_3 disappear (Fig.5a), while those of $Fe_{1.7}Mn_{0.3}O_3$ remain as the 2nd ones (Fig. 5b).

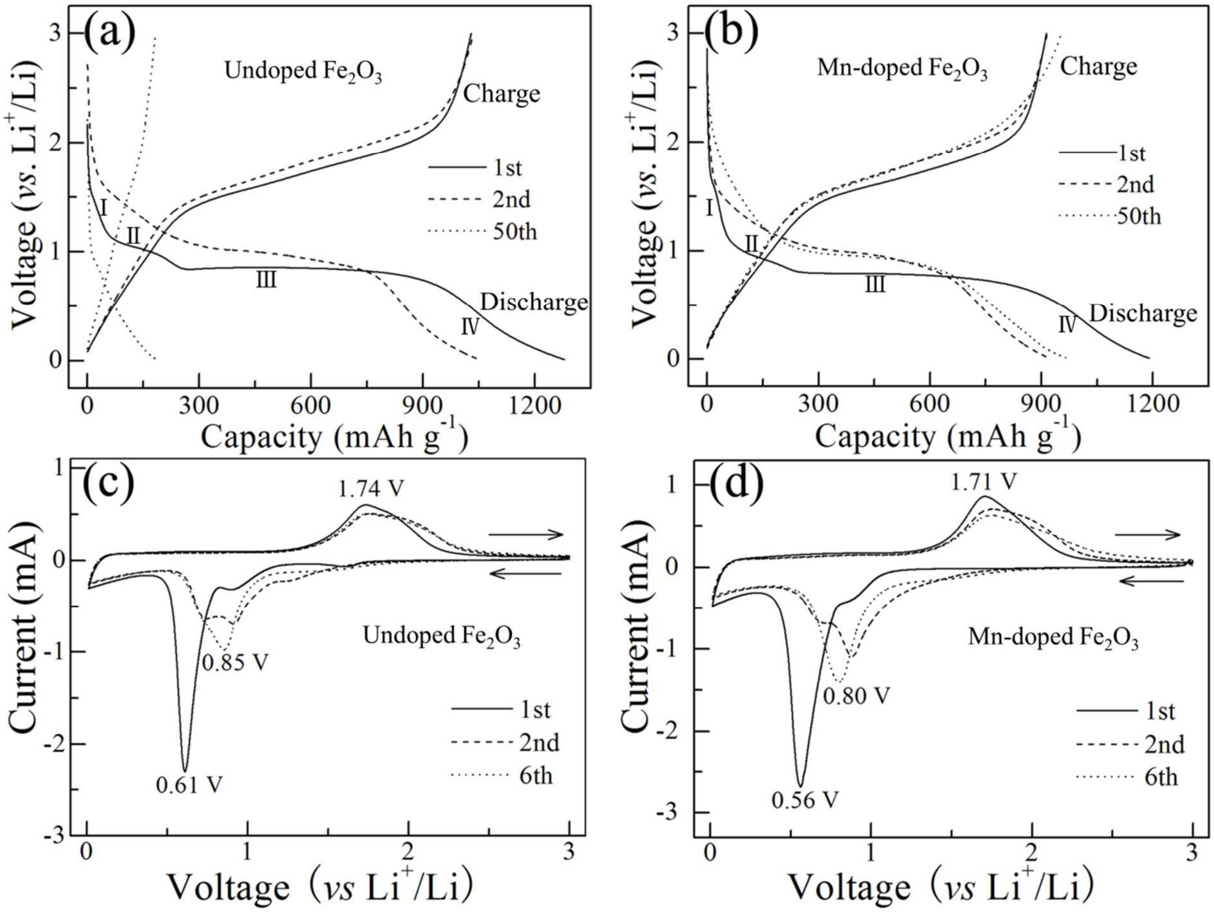

Fig. 5 (a, b) Discharge-charge profiles and (c, d) CV curves of undoped and Mn-doped α-Fe_2O_3 electrodes operated at a current density of 200 mA g^{-1} and at a scanning rate of 0.1 mV s^{-1}, respectively.

As shown in Fig. 5a, pure α-Fe_2O_3 delivers the 1st and 50th specific discharge capacities of

~1280 and 178 mAh g^{-1}. In contrast to these, the effectively doped $Fe_{1.7}Mn_{0.3}O_3$ exhibits the relatively low initial discharge capacity of ~1190 mAh g^{-1} but the extremely high reversible value of ~970 mAh g^{-1} in the 50th cycle (Fig. 5b). In view of the similar structural properties of undoped and Mn-doped samples (e.g., a shape of hollow quadrangular prism and a close value of specific surface area), the much higher value of the 50th reversible capacity of Mn-doped α-Fe_2O_3 indicates the positive effect of elemental doping on the electrochemical durability of α-Fe_2O_3.

At 0.1 mV s^{-1} the CV behaviors of pure α-Fe_2O_3 are presented in Fig. 5c, showing the same redox reaction information as literature reports.[15,21,25,26] In comparison with the CV behaviors of Mn-doped α-Fe_2O_3 (Fig. 5d), each anodic/cathodic peaks of pure α-Fe_2O_3 appears at a relatively high voltage as labeled in Fig. 5c. It should also be mentioned that, at 6th CV cycle and thereafter, there is almost no position shift of these peak voltages for both undoped and Mn-doped α-Fe_2O_3 (Fig. 5c, d). Anyway, by comparison the relatively low-potential positions and high-current intensities of Mn-doped electrode do not mean that the effective doping of elemental Mn can improve the electrochemical reversibility between α-Fe_2O_3 and metallic Fe^0.

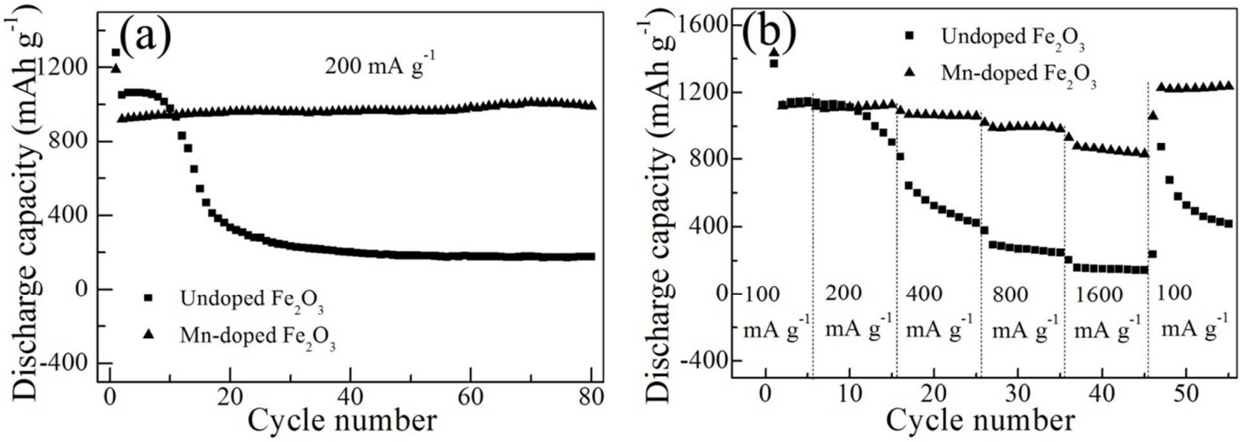

Fig. 6 (a) Cycling stabilities and (b) rate performances of undoped and Mn-doped α-Fe_2O_3 electrodes operated at different current rates.

Within the voltage range of 0.01-3 V, cycling performances of undoped and Mn-doped Fe_2O_3 electrodes were comparatively measured at 200 mA g^{-1}. As shown in Fig. 6a, pure α-Fe_2O_3 delivers the 1st and 10th discharge capacity of ~1280 and 1015 mAh g^{-1} and then it experiences a dramatic capacity loss to ~178 mAh g^{-1} after 80 cycles. When elemental Mn was effectively incorporated into the lattice structure of rhombohedral α-Fe_2O_3, the resulting $Fe_{1.7}Mn_{0.3}O_3$ delivers the 2nd discharge capacity of ~922 mAh g^{-1} and then keeps the slightly increasing tendency of capacity to 1000 mAh g^{-1} after 80 cycles (Fig. 6a). In fact, the slight increasing of discharge capacity has been observed for other transition oxides and therein this has been reasonably attributed to a reversible formation-dissolution of polymeric gel-like layer outside the particles' surface.[37,38] Perhaps, this phenomenon could explain the reason why the introduction of appropriate amount of Mn(III) into crystalline α-Fe_2O_3 seemingly improves the electrochemical reversibility between α-Fe_2O_3 and metallic Fe^0.

At different current densities from 100 to 1600 mA g^{-1}, rate capabilities of the two electrodes have also been performed to examine the doping effect of elemental Mn (Fig. 6b). By contrast, the high-rate capability of $Fe_{1.7}Mn_{0.3}O_3$ is as superior as its low-rate cycleability shown in Fig. 6a, giving the average discharge capacities of ~1130, 1070 and 852 mAh g^{-1} at 100, 400 and 1600 mA g^{-1}, respectively. When current density returns from 1600 to 100 mA g^{-1}, the discharge capacity recovers to a high value of ~1237 mAh g^{-1}. From Fig. 6b, the observed discharge capacities of $Fe_{1.7}Mn_{0.3}O_3$ at each current rate are correspondingly higher than those of pure α-Fe_2O_3, indicate a positive effect of Mn (III) ions on the rate performances of Mn-doped α-Fe_2O_3 especially at a high current density (Fig. 6b).

Generally, an effective coating of carbonaceous materials can improve the electrochemical durability of transition metal oxides, however, this could involuntarily “modify” elemental valences of Fe (III) (e.g., $Fe_2O_3 \rightarrow Fe_3O_4$) or Mn(III) (i.e., $Mn_2O_3 \rightarrow MnO$).[24,39] This may change potential barriers for the electrochemical transformation of M_xO_y to M^0 (M, a transition metal), although the electrocatalytic activity of in situ formed metallic M^0 nanoparticles have been well demonstrated previously.[40-42] Owing to the binary reversible reactions of “$M_2O_3 \leftrightarrow M^0$, M = Fe-Mn” occurring at different potentials in sequence, the less capacity fade of Mn-doped α-Fe_2O_3 during continuous discharge-charge processes may be explained by the mutually electrocatalytic activities of metallic Fe^0 and Mn^0 comparing with that of pure α-Fe_2O_3.

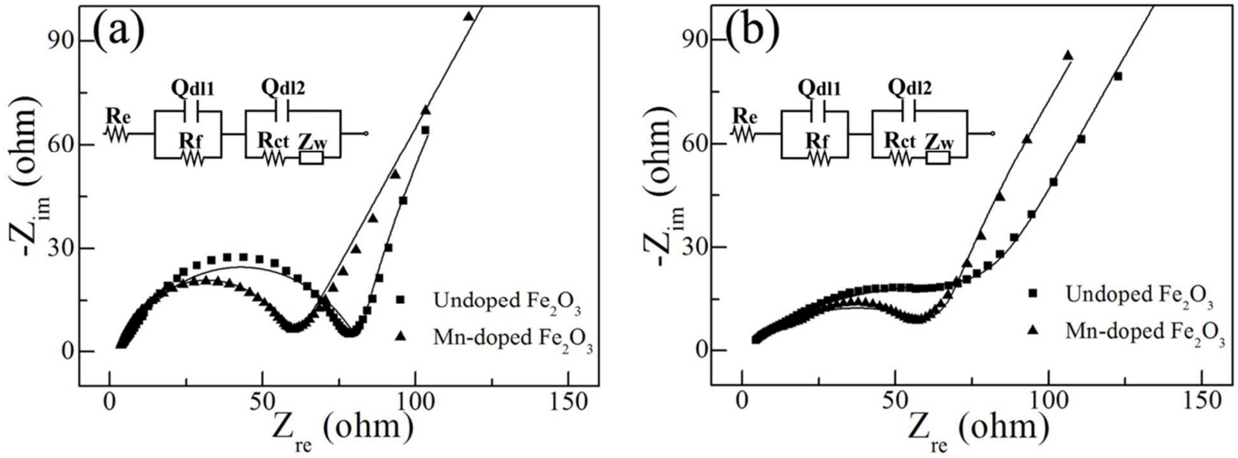

Fig. 7 Nyquist plots (symbols) and the fitted profiles (lines) of undoped and Mn-doped α-Fe_2O_3 electrodes operated at different states: (a), prior to electrochemical cycling; (b), after 25 discharge-charge cycles at 200 mA g^{-1}. Insets are the corresponding equivalent circuits.

To compare the charge transport kinetics of undoped and Mn-doped α-Fe_2O_3 electrodes, EIS measurements were carried out at different electrochemical cycling states. As shown in Fig. 7a or b, EIS results of the comparative electrodes can be fitted using an equivalent circuit at each operating state. According to this equivalent circuit, their approximate charge transport kinetics are too complicated to explain, anyway, therein the marked electrochemical parameters R_e, R_f, R_{ct}

and Z_W represent electrolyte resistance, surface film resistance, Li-ion charge transfer resistance and Warburg impedance in sequence. All the Nyquist plots contains a depressed semicircle in high and medium frequency region and a low frequency linear tail, which are indicative of charge-transfer impedance (R_{ct}) on electrode-electrolyte interface and Warburg impedance (Z_W) related to Li-ion diffusion kinetics, respectively.[29,33,40,43]

It is well-known that the smaller the charge transfer resistance and the smaller the diameter of the semicircle. When operated at an open-circuit voltage state, the Nyquist plot of fleshly assembled Mn-doped α-Fe_2O_3 electrode displays a smaller semicircle than that of fleshly assembled pure α-Fe_2O_3 electrode, comparatively giving the estimated R_{ct} values of 56 and 78 Ω in sequence. Over 25 discharge-charge cycles at 200 mA g^{-1} (Fig. 7b), the obtained R_{ct} value of $Fe_{1.7}Mn_{0.3}O_3$ (73 Ω) is still smaller than that of undoped α-Fe_2O_3 (105 Ω). Therefore, the incorporation of elemental Mn into crystalline α-Fe_2O_3 can improve the charge transfer ability of Li^+-ions and/or electrons across the interface between electrolyte and electrode.

4. Conclusions

In summary, the initial oxalate co-precipitation at room temperature and subsequent thermal decomposition at 600 °C facilitate both the effective incorporation of Mn(III) ions into the lattice structure of rhombohedral α-Fe_2O_3 and the controlling synthesis of Mn-doped α-Fe_2O_3 hollow quadrangular prisms with a porous shell. When applied as LIB anodes, the electrochemical properties (e.g., cycling stability, rate capability and the charge transfer resistance for Li^+-ion diffusion) of nanostructured $Fe_{1.7}Mn_{0.3}O_3$ are better than those of pure α-Fe_2O_3. For potential application purposes, an optimal amount of doping Mn(III) ions and the plausible reversible reaction mechanism of Mn-doped α-Fe_2O_3 towards metal lithium deserve to be conducted in future.

Acknowledgments

The authors thank the financial supports from the National Basic Research Program of China (2011CB935900), from Shandong Province (ZR2012BM001) and from Shandong University (2014JC016).

References

(1) Y. G. Guo, J. S. Hu, L.J. Wan, *Adv. Mater.*, 2008, **20**, 2878-2887.

(2) M. Armand, J. M. Tarascon, *Nature*, 2008, **451**, 652-657.

(3) F.Y. Cheng, J. Liang, Z.L. Tao, J. Chen, *Adv. Mater.*, 2011, **23**, 1695-1715.

(4) J. Cabana, L. Monconduit, D. Larcher, M.R. Palacín, *Adv. Mater.*, 2010, **22**, E170-E192.

(5) J. Chen, L.N. Xu, W.Y. Li, X. L. Gou, *Adv. Mater.*, 2005, **17**, 582-586.

(6) K. F. Zhong, X. Xia, B. Zhang, H. Li, Z. X. Wang, L.Q. Chen, *J. Power Sources*, 2010, **195**, 3300-3308.

(7) X. Wang, X. L. Wu, Y. G. Guo, Y. T. Zhong, X. Q. Cao, Y. Ma, J. N. Yao, *Adv. Funct. Mater.*, 2010, **20**, 1680-1686.

(8) Y. F. Deng, Z. E. Li, Z. C. Shi, H. Xu, F. Peng, G. H. Chen, *RSC Adv.*, 2012, **2**, 4645-4647.

(9) J. J. Zhang, Y. L. Chen, Y. F. Sun, T. Huang, A. S. Yu, *RSC Adv.*, 2013, **3**, 20639-20646.

(10) Y. F. Deng, L. N. Wan, Y. Xie, X. S. Qin, G. H. Chen, *RSC Adv.*, 2014, **4**, 23914-23935.

(11) Y. Q. Song, S. S. Qin, Y. W. Zhang, W. Q. Gao, J. P. Liu, *J. Phys. Chem. C*, 2010, **114**,

21158-21164.

(12) J. M. Ma, J. B. Lian, X. C. Duan, X. D. Liu, W. J. Zheng, *J. Phys. Chem. C*, 2010, **114**, 10671-10676.

(13) H. Liu, G. X. Wang, J. Park, J. Z. Wang, H. K. Liu, C. Zhang, *Electrochim. Acta*, 2009, **54**, 1733-1736.

(14) M. V. Reddy, T. Yu, C.H. Sow, Z. X. Shen, C. T. Lim, G. V. Subba Rao, B. V. R. Chowdari, *Adv. Funct. Mater.*, 2007, **17**, 2792-2799.

(15) Y. N. NuLi, R. Zeng, P. Zhang, Z. P. Guo, H. K. Liu, *J. Power Sources*, 2008, **184**, 456-461.

(16) X. L. Wu, Y. G. Guo, L. J. Wan, C. W. Hu, *J. Phys. Chem. C*, 2008, **112**, 16824-16829.

(17) B. Sun, J. Horvat, H. S. Kim, W. S. Kim, J. Ahn, G. X. Wang, *J. Phys. Chem. C*, 2010, **114**, 18753-18761.

(18) X. D. Xu, R. G. Cao, S. Jeong, J. Cho, *Nano Lett.*, 2012, **12**, 4988-4991.

(19) X. Y. Yao, C. L. Tang, G. X. Yuan, P. Cui, X. X. Xu, Z. P. Liu, *Electrochem. Commun.*, 2011, **13**, 1439-1442.

(20) Z. C. Wu, K. Yu, S. D. Zhang, Y. Xie, *J. Phys. Chem. C*, 2008, **112**, 11307-11313.

(21) S. L. Chou, J. Z. Wang, D. Wexler, K. Konstantinov, C. Zhong, H. K. Liu, S. X. Dou, *J. Mater. Chem.*, 2010, **20**, 2092-2098.

(22) M. F. Hassan, M. M. Rahman, Z. P. Guo, Z. X. Chen, H. K. Liu, *Electrochim. Acta*, 2010, **55**, 5006-5013.

(23) W. J. Yu, P. X. Hou, L. L. Zhang, F. Li, C. Liu, H. M. Cheng, *Chem. Commun.*, 2010, **46**, 8576-8578.

(24) F. F. Xu, W. P. Kang, X. X. Wang, R. Liu, C. H. Zhao, Q. Shen, *CrystEngComm*, 2013, **15**,

4431-4437.

(25) Y. Q. Zou, J. Kan, Y. Wang, *J. Phys. Chem. C*, 2011, **115**, 20747-20753.

(26) G. W. Zhou, J. Wang, P. Gao, X. Yang, Y. S. He, X. Z. Liao, J. Yang, Z. F. Ma, *Ind. Eng. Chem. Res.*, 2013, **52**, 1197-1204.

(27) S. Bai, S. Q. Chen, X. P. Shen, G. X. Zhu, G. X. Wang, *RSC Adv.*, 2012, **2**, 10977-10984.

(28) D. Pasero, N. Reeves, A. R. West, *J. Power Sources*, 2005, **141**, 156-158.

(29) Y. J. Mai, J. P. Tu, X. H. Xia, C. D. Gu, X. L. Wang, *J. Power Sources*, 2011, **196**, 6388-6393.

(30) Q. Li, L. W. Yin, Z. Q. Li, X. K. Wang, Y. X. Qi, J. Y. Ma, *ACS Appl. Mater. Interfaces*, 2013, **5**, 10975-10984.

(31) K. M. Nam, Y. C. Choi, S. C. Jung, Y. I. Kim, M. R. Jo, S. H. Park, Y. M. Kang, Y. K. Han, J. T. Park, *Nanoscale*, 2012, **4**, 473-477.

(32) H. Yu, X. H. Rui, H. T. Tan, J. Chen, X. Huang, C. Xu, W. L. Liu, D. Y. W. Yu, H. H. Hng, H. E. Hoster, Q. Y. Yan, *Nanoscale*, 2013, **5**, 4937-4943.

(33) L. T. Anh, A. K. Rai, T. V. Thi, J. Gim, S. Kim, V. Mathew, J. Kim, *J. Mater. Chem. A*, 2014, **2**, 6966-6975.

(34) H. Pang, S. M. Wang, X. X. Li, S. S. Zhao, N. N. Zhang, J. Chen, J. S. Zhang, H. H. Zheng, S. J. Li, *Int. J. Electrochem. Sci.*, 2013, **8**, 4174-4182.

(35) M. C. López, J. L. Tirado, C. P. Vicente, *J. Power Sources*, 2013, **227**, 65-71.

(36) W. A. Ang, N. Gupta, R. Prasanth, S. Madhavi, *ACS Appl. Mater. Interfaces*, 2012, **4**, 7011-7019.

(37) K. M. Shaju, F. Jiao, A. Débart, P. G. Bruce, *Phys. Chem. Chem. Phys.*, 2007, **9**, 1837-1842.

(38) C. C. Li, Q. H. Li, L. B. Chen, T. H. Wang, *J. Mater. Chem.*, 2011, **21**, 11867-11872.

(39) T. Li, Y. Y. Wang, R. Tang, Y. X. Qi, N. Lun, Y. J. Bai, R. H. Fan, *ACS Appl. Mater. Interfaces*, 2013, **5**, 9470-9477.

(40) Y. Ma, C. L. Fang, B. Ding, D. Ji, J. Y. Lee, *Adv. Mater.*, 2013, **25**, 4646-4652.

(41) W. P. Kang, F. L. Liu, Y. L. Su, D. J. Wang, Q. Shen, *CrystEngComm*, 2011, **13**, 4174-4180.

(42) L. W. Su, Y. R. Zhong, Z. Zhou, *J. Mater. Chem. A*, 2013, **1**, 15158-15166.

(43) Y. Ma, C. Zhang, G. Ji, J. Y. Lee, *J. Mater. Chem.*, 2012, **22**, 7845-7850.